THE UNIVERSITY of EDINBURGH

Edinburgh Research Explorer

Charge Transport in UV-Oxidized Graphene and Its Dependence on the Extent of Oxidation

OPEN ACCESS

Article

Charge Transport in UV-Oxidized Graphene and Its Dependence on the Extent of Oxidation

Hwa Yong Lee [1], Mohd Musaib Haidari [1], Eun Hee Kee [1], Jin Sik Choi [1], Bae Ho Park [1], Eleanor E. B. Campbell [2] and Sung Ho Jhang [1,*]

1 School of Physics, Konkuk University, Seoul 05029, Korea
2 EaStCHEM, School of Chemistry, Edinburgh University, David Brewster Road, Edinburgh EH9 3FJ, UK
* Correspondence: shjhang@konkuk.ac.kr

Abstract: Graphene oxides with different degrees of oxidation are prepared by controlling UV irradiation on graphene, and the charge transport and the evolution of the transport gap are investigated according to the extent of oxidation. With increasing oxygenous defect density n_D, a transition from ballistic to diffusive conduction occurs at $n_D \simeq 10^{12}$ cm^{-2} and the transport gap grows in proportion to $\sqrt{n_D}$. Considering the potential fluctuation related to the $e - h$ puddle, the bandgap of graphene oxide is deduced to be $E_g \simeq 30\sqrt{n_D \, (10^{12} \text{ cm}^{-2})}$ meV. The temperature dependence of conductivity showed metal–insulator transitions at $n_D \simeq 0.3 \times 10^{12}$ cm^{-2}, consistent with Ioffe–Regel criterion. For graphene oxides at $n_D \geq 4.9 \times 10^{12}$ cm^{-2}, analysis indicated charge transport occurred via 2D variable range hopping conduction between localized sp^2 domain. Our work elucidates the transport mechanism at different extents of oxidation and supports the possibility of adjusting the bandgap with oxygen content.

Keywords: graphene oxide; defect density; transport gap; band gap; metal–insulator transition; 2D Mott VRH

1. Introduction

Graphene is a two-dimensional semimetal with high conductivity and mobility [1,2], and is a promising candidate for applications within electronics and optoelectronics. However, a bandgap E_g is required for certain applications and various methods have been attempted to controllably induce a bandgap in graphene. While a confinement-induced bandgap is widely investigated in graphene nanoribbons [3], a bandgap can also be induced by breaking the symmetry of the graphene lattice. As an approach to break the symmetry, functionalization of graphene with foreign atoms [4–6] such as oxygen, fluorine, and hydrogen has been tested to open a finite bandgap. For graphene oxide (GO), the bandgap is suggested to be tuned by the extent of oxidation, and $E_g \simeq 2.6$–6.5 eV is theoretically expected for fully oxidized graphene (O/C = 50%) [7–10].

The most common method to produce GO is based on wet chemistry, consisting of oxidation of graphite in strong acids, followed by a liquid exfoliation [4,11]. The degree of oxidation can be tuned by subsequent reduction via thermal or chemical treatment [12], and the transition from insulator to semimetal with increasing reduction of GO has been reported [13,14]. Despite the advantage for large-scale production of GO, this production method introduces contamination, and alternative dry oxidation methods such as plasma [4,15] and UV treatments [16,17] have been developed. Plasma oxidation produces GO by exposing graphene to an oxygen plasma, and the semimetallic graphene undergoes a transition into an insulator according to the time of exposure to the plasma [9,18]. UV/ozone treatment also controls the degree of oxidation of graphene with UV exposure time, and both methods provide convenient control over the extent of oxidation. In addition, UV oxidation causes less distortion of the graphene lattice [19,20] compared to the energetic plasma collisions that can introduce topological defects.

Transport studies of GO and observation of metal–insulator transition via oxidation or reduction reactions have been reported [9,13,14,18], but a systematic study of the transport mechanism and evolution of the transport gap for different degrees of oxidation is still required. In this paper, we produced GO samples with different extents of oxidation through UV treatment and systematically investigated the transport mechanism and the evolution of the transport gap across the metal–insulator transition.

2. Experimental

Our experiments were conducted on seven graphene field-effect-transistors (FETs) fabricated using exfoliated graphene on SiO_2 (300 nm)/Si substrates, and a device with Hall-bar geometry using graphene grown by chemical vapor deposition. For all devices, Pd (20 nm)/Au (20 nm) electrodes were deposited by e-beam lithography. Typical images of the devices are shown in Figure 1a,b. For those seven FETs prepared using exfoliated graphene, the size of the channel was unified to 2 μm × 2 μm (width × length) via oxygen plasma etching to compare later the characteristics depending on the extent of the graphene oxidation. The graphene devices were then oxidized by irradiating UV with a wavelength of 172 nm at an intensity of 20 mW/cm^2 under ambient conditions (humidity with 30 to 40%). The extent of oxidation was roughly controlled by the irradiation time. Among seven graphene FETs, groups of two devices were exposed to UV light for 15, 20, and 25 s, respectively, leaving one pristine graphene FET for reference. A laser with excitation energy of 2.33 eV was used to obtain Raman spectra of the oxidized graphene. Charge transport characteristics of the seven FETs were studied using a vacuum probe station and a Keithley 4200 semiconductor characterization system in Core Facility Center for Quantum Characterization/Analysis of Two-Dimensional Materials & Heterostructures for the temperature $77 < T < 400$ K. The graphene device with Hall-bar geometry was investigated after UV oxidation by using a quantum design PPMS for lower T down to 2 K and magnetic fields up to 7 tesla.
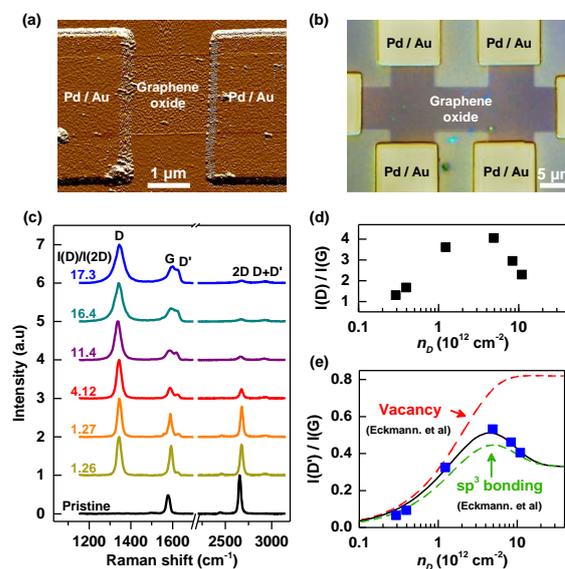
Figure 1. (**a**) Atomic force microscope image of a typical graphene FET, irradiated with UV for oxidation. (**b**) Optical image of a CVD-grown graphene device with Hall-bar geometry. (**c**) The evolution of Raman spectra of graphene devices exposed to UV light arranged according to the value of $I(D)/I(2D)$. (**d**) Values of n_D deduced from $I(D)/I(G)$ for six graphene devices irradiated with UV (**e**) $I(D')/I(G)$ as a function of n_D. The black solid line is a fit to Equation (2). Dashed lines are the evolution of $I(D')/I(G)$ either for vacancies or sp^3 sites, suggested from Ref. [21].

3. Result and Discussion

Figure 1c presents Raman spectra of pristine graphene and six graphene FETs exposed to UV light for 15, 20, or 25 s. Defect-activated D ($\sim$1345 cm^{-1}), D' ($\sim$1625 cm^{-1}), and $D + D'$ ($\sim$2930 cm^{-1}) peaks appeared for the graphene samples irradiated with UV, in addition to G ($\sim$1580 cm^{-1}) and $2D$ ($\sim$2650 cm^{-1}) peaks of pristine graphene [22]. The two graphene FETs irradiated for the same time resulted in rather different Raman spectra, possibly due to the different degrees of PMMA residues remaining on the graphene samples. Hence, in Figure 1c, Raman spectra were arranged with respect to the ratio between the D and the $2D$ peak intensities, $I(D)/I(2D)$, as the rise of D and the suppression of $2D$ peaks with increasing defect density were reported extensively as a means of quantifying defective graphene including graphene oxide [21,23–25]. Previous works on defective graphene introduced the local activation model to explain the evolution of Raman spectra, and in this model the ratio between the D and G peak intensities, $I(D)/I(G)$, allows us to estimate the defect density n_D, which corresponds to the degree of oxidation in our experiments [21],

$$\frac{I(D)}{I(G)} = C_{A,D} \frac{r^2_{A,D} - r^2_{S,D}}{r^2_{A,D} - 2r^2_{S,D}} \left[e^{-\pi^2 r^2_{S,D}\ n_D} - e^{-\pi^2 (r^2_{A,D} - r^2_{S,D})\ n_D} \right] \tag{1}$$

Here, $C_{A,D}$ is a parameter related to the electron–phonon coupling of the D peak phonon, and $r_{S,D}$ and $r_{A,D}$ are values that indicate the size of the defect site. To deduce n_D, we assumed $C_{A,D} = 6$, which agrees well with the excitation laser of 532 nm and the maximum value of $I(D)/I(G) \simeq 4$ observed in our experiment [26,27] with $r_{S,D} = 1$ nm and $r_{A,D} = 3$ nm [21]. As shown in Figure 1d, values of n_D are deduced to be between 0.29 and 11 ($\times 10^{12}$ cm^{-2}) for the graphene samples irradiated with UV light.

To discuss the nature of the defects, we now inspect the ratio between the D' and the G peak intensities, $I(D')/I(G)$, which is sensitive to the nature of the defect. Figure 1e shows $I(D')/I(G)$ as a function of n_D estimated for the six irradiated graphene samples. For low defect densities, $I(D')/I(G)$ increases with n_D, and then starts to decrease for $n_D \geq 4.9 \times 10^{12}$ cm^{-2} presenting a maximum value of $\simeq 0.5$. The ratio between the D' and the G peak intensities can be fitted with the following Equation (2).

$$\frac{I(D')}{I(G)} = C_{A,D'} \frac{r^2_{A,D'} - r^2_{S,D'}}{r^2_{A,D'} - 2r^2_{S,D'}} \left[e^{-\pi^2 r^2_{S,D'}\ n_D} - e^{-\pi^2 (r^2_{A,D'} - r^2_{S,D'})\ n_D} \right]$$
$$+ C_S \left(1 - e^{-\pi^2 r^2_{S,D'}\ n_D} \right) \tag{2}$$

Here, C_S is a parameter related to the defect type and $C_{A,D'}$ is a parameter related to the electron–phonon coupling of the D' peak phonon, with $r_{A,D'}$ and $r_{S,D'}$ being the length scales of the defect sites. Our data are best fitted with Equation (2) (solid line) when $C_S = 0.33$ and $C_{A,D'} = 0.63$ (Figure 1e). Eckmann et al. [21] derived from their experiments $C_S = 0.33$ for sp^3 sites and $C_S = 0.82$ for vacancies. Excellent agreement with $C_S = 0.33$ suggests the oxidation of our graphene through UV treatment, forms sp^3 bonds. Dashed lines in Figure 1e show the evolution of $I(D')/I(G)$ for graphene with either vacancies or sp^3 sites, calculated with $C_{A,D'} = 0.5$, $r_{S,D'} = 1.4$ nm and $r_{A,D'} = 2.6$ nm from ref. [21]. Note the slight mismatch with the curve for sp^3 sites is due to the different value of $C_{A,D'}$ determined for our samples.

Regarding n_D as an oxygenous defect density and a measure of the degree of oxidation of graphene, we investigate the charge transport characteristics depending on n_D in oxidized graphene devices. Figure 2 displays transfer characteristics of the oxidized graphene FETs at different n_D, measured with a fixed drain-source bias V_{DS} of 1 mV. A back-gate voltage V_g is applied over the 300 nm thick SiO$_2$, and the carrier density n is given by $n = \alpha(V_g - V_{CNP})$ with $\alpha = 7.2 \times 10^{10}$ cm^{-2} using the parallel capacitor model [28]. Here, V_{CNP} is the voltage at the charge-neutrality point. The conductivity σ monotonically decreases with increasing n_D. Compared to the pristine graphene, the conductivity of

oxidized graphene is, for example, $\sim$1000 times smaller at $n_D = 11 \times 10^{12}$ cm^{-2}. In addition, the conductivity becomes flattened near $n = 0$ with increasing n_D, discussed in terms of the so-called "transport gap" in the next paragraph. We also note for samples with $n_D < 10^{12}$ cm^{-2} it follows $\sigma \propto \sqrt{n}$ (Figure 2a,b), while for $n_D > 10^{12}$ cm^{-2} it shows $\sigma \propto n$ outside the flat area (Figure 2c–f). This behavior implies that charge transport transitioned from ballistic to diffusive transport at the oxidation density of $n_D \simeq 10^{12}$ cm^{-2}. It is known that $\sigma \propto \sqrt{n}$ in ballistic graphene [28,29] and $\sigma \propto n$ in diffusive graphene [30,31]. The estimation of the mean free path $l = \frac{\sigma h}{2e^2} \cdot \frac{1}{\sqrt{\pi n}}$ [28,32] gives $l \simeq 4$ μm for our pristine graphene and $l \simeq 1.5$ μm for the GO FET with $n_D = 0.39 \times 10^{12}$ cm^{-2}, which are twice as large and comparable to the channel length (2 μm), respectively. Additionally, $l \simeq 600, 130,$ and 5 nm, estimated for GO FETs with $n_D = 1.2, 4.9,$ and 11 ($\times 10^{12}$ cm^{-2}), respectively, meet the condition for diffusive transport ($l <$ channel length), consistent with our observation.
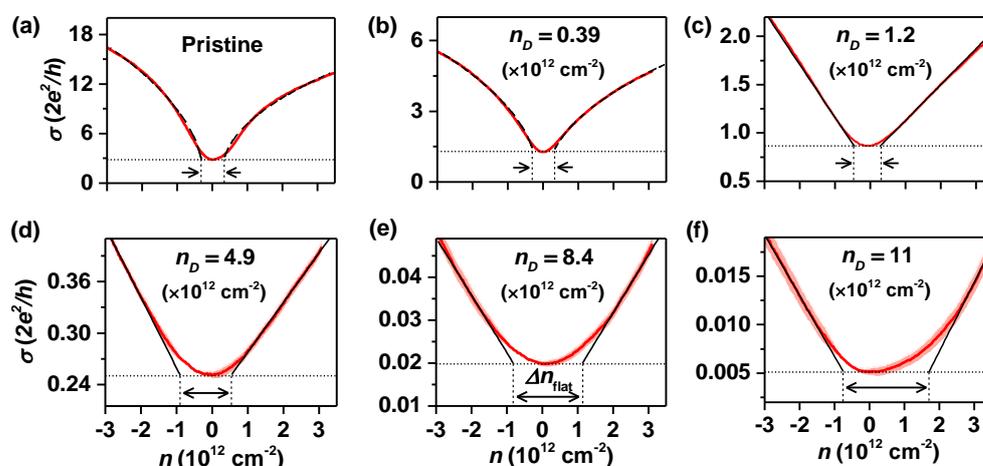
Figure 2. Transfer curves of oxidized graphene FETs with different n_D. The red shade shows the standard deviation of repeated measurements. (**a**) pristine graphene; (**b**) $n_D = 0.39 \times 10^{12}$ cm^{-2}; (**c**) $n_D = 1.2 \times 10^{12}$ cm^{-2}; (**d**) $n_D = 4.9 \times 10^{12}$ cm^{-2}; (**e**) $n_D = 8.4 \times 10^{12}$ cm^{-2}; (**f**) $n_D = 11 \times 10^{12}$ cm^{-2}. Black dotted lines show the minimum conductivity σ_{min}. Dashed lines in (**a**,**b**) are fits to $\sigma \propto \sqrt{n}$, and solid lines in (**c**–**f**) are linear fits to the transfer curves. With increasing n_D, transfer curve becomes more flattened near $n = 0$, as indicated by the width Δn_{flat}.

The change in the transport mechanism observed in GO FETs happens because the scattering with oxygenous defects becomes more frequent as the extent of the oxidation increases. Figure 3a shows how the conductivity minimum σ_{min} and electron side mobility μ_e are reduced with increasing extent of oxidation. Field-effect mobility estimated from the electron side ($\mu_e = \frac{1}{e} \cdot \frac{d\sigma}{dn}$ [24]), decreases from $\mu_e \sim 2900$ (pristine) to ~ 500 ($n_D = 0.29 \times 10^{12}$ cm^{-2}) and ~ 3.6 cm^2/V·s ($n_D = 11 \times 10^{12}$ cm^{-2}) with increasing n_D. These results are also consistent with $\mu \simeq 30 - 2$ cm^2/V·s, reported for reduced graphene oxides at $n_D \simeq 5 - 11$ ($\times 10^{12}$) cm^{-2}, synthesized by using a modified Hummer's method [26,33]. On the other hand, with the oxidation of graphene, the bandgap opens and disorder-induced localized states appear inside the bandgap, resulting in a transport gap Δ_m related to Δn_{flat} in Figure 2 [34,35]. To discuss the dependence of the transport gap on the oxygen content, we display in Figure 3b the flattened width Δn_{flat}, observed in Figure 2, as a function of n_D. Δn_{flat} gradually increases with n_D, while $\Delta n_{\text{flat}} = 0.42 \times 10^{12}$ cm^{-2} for pristine graphene, associated with residual carrier densities n_0 originating from the electron(e)–hole(h) puddle [36]. The transport gap, estimated from $\Delta_m = \hbar v_F \sqrt{\pi \Delta n_{\text{flat}}}$ [37–39], overestimates the actual bandgap due to the existence of disorder potentials near the charge neutrality point ($e - h$ puddle), as illustrated in Figure 3c. Taking into account the potential fluctuation related to the $e - h$ puddle, $\delta E_{e-h} = \hbar v_F \sqrt{\pi \Delta n_0} \simeq 78$ meV from the pristine graphene device, we can infer the bandgap of UV-oxidized graphene at the different oxygenous defect densities. With $E_g \simeq \Delta_m - \delta E_{e-h}$, the inferred bandgap is presented as a function of

n_D in Figure 3d, together with the transport gap observed, Δ_m. E_g is seen to increase in proportion to $\sqrt{n_D}$, according to the relationship $E_g \simeq 30\sqrt{n_D \ (10^{12} \ \mathrm{cm}^{-2})}$ meV. Substitution of $n_D \simeq 1.9 \times 10^{15}$ cm^{-2} for fully oxidized graphene C$_2$O (epoxide) results in $E_g \simeq 1.3$ eV, comparable to $E_g \simeq 2.6$–6.5 eV calculated from theory for fully oxidized graphene [7–10]. Our results support the possibility of continuously adjusting the bandgap by tuning the oxygen content.
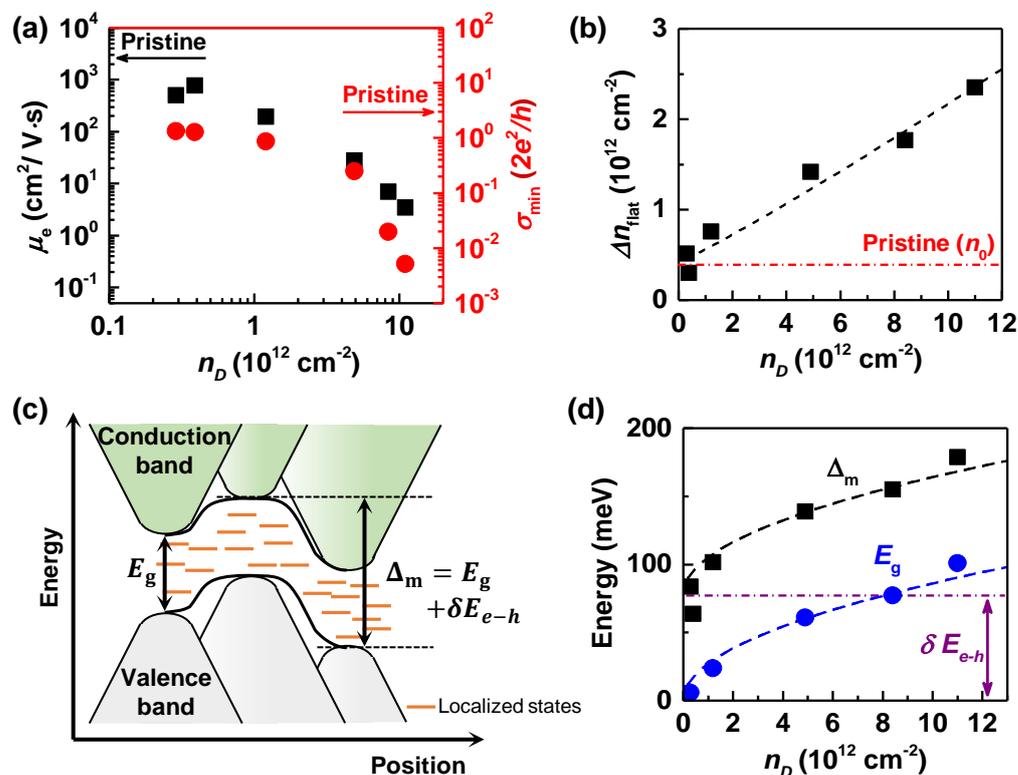

Figure 3. (**a**) Electron side mobility μ_e (black square) and conductivity minimum σ_{min} (red circle) of graphene oxide as a function of n_D. Arrows indicate the values of μ_e and σ_{min} for pristine graphene. (**b**) Δn_{flat} versus n_D. The black dashed line is a linear fit to the data. Note y-intercept n_0, associated with the electron–hole puddle in pristine graphene. (**c**) Schematic band diagram of graphene oxide and the illustration of an electron-hole puddle, affecting the transport gap observed. (**d**) Transport gap (black square) and inferred bandgap (blue circle) of graphene oxide as a function of n_D. Dashed lines are fitting curves with $\sqrt{n_D}$ and the dot-dash line indicates the size of potential fluctuation due to $e-h$ puddle.

Figure 4 shows the temperature T dependence of σ_{min} for graphene oxide with different values of n_D, studied for $77 < T < 400$ K. Pristine graphene exhibits metallic behavior in which σ_{min} decreases with T. For GO samples with $n_D = 0.29$ and 0.39 ($\times 10^{12}$ cm^{-2}), conductivity minimum slightly increases with T, and the insulating behavior develops further with increasing n_D. The metal–insulator transition appears for $k_F l = 1$ and meets the Ioffe–Regel criterion, where k_F is the Fermi wavenumber and l is the mean free path with $k_F l = \sigma_{min} \frac{h}{2e^2}$ [40]. Considering $E_g \simeq 60$ meV for GO at $n_D \simeq 5 \times 10^{12}$ cm^{-2}, inferred from Figure 3d, the pronounced insulating behavior observed for $n_D \geq 4.9 \times 10^{12}$ cm^{-2} reflects that the size of opened bandgap becomes larger than the thermal energy ($\sim$26 meV at room temperature).
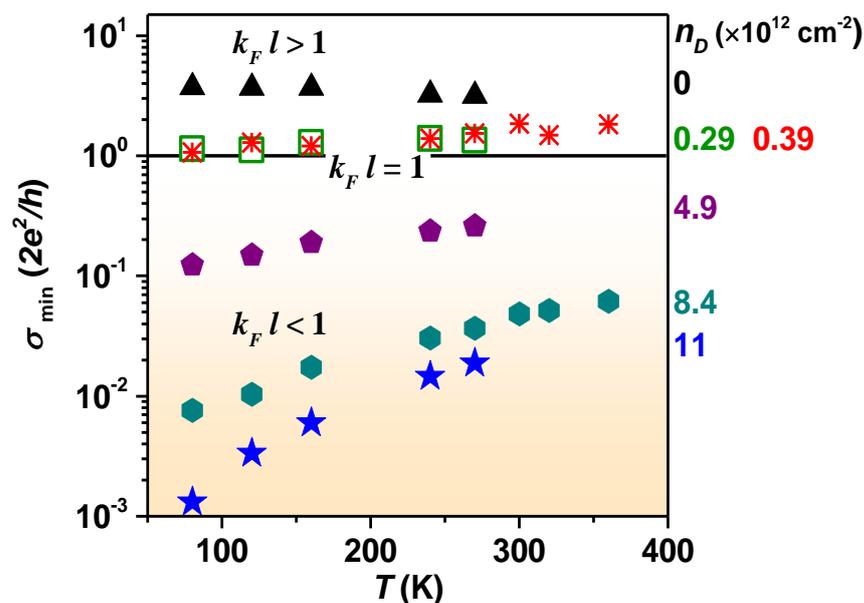
Figure 4. Temperature dependence of conductivity minimum for graphene oxides with different n_D. Solid line indicates $k_F l = 1$.

In Figure 5a, analysis shows the charge transport in GO samples for larger n_D = 4.9, 8.4, and 11×10^{12} cm^{-2} is localized and the T-dependence of $\sigma_{\min}$ is well explained by 2D Mott variable range hopping conduction (2D VRH) [14,41], following $\sigma = \sigma_0 \exp\left(\frac{T_0}{T}\right)^{\frac{1}{3}}$. Note that $\log \sigma_{\min}$ is linear with $T^{-1/3}$ in Figure 5a. Characteristic temperature $T_0 = 900$, 17,000, and 41,000 K are obtained from the linear fits for $n_D = 4.9$, 8.4, and 11×10^{12} cm^{-2}, respectively. The localization length $\xi = \sqrt{\frac{13.8}{k_B \mathrm{DOS}(E) T_0}}$, estimated for $0 < n < 3 \times 10^{12}$ cm^{-2}, decreases from 32–46 nm ($n_D = 4.9$) and 9–17 nm ($n_D = 8.4$) to 6–11 nm ($n_D = 11 \times 10^{12}$ cm^{-2}) with increasing n_D. Here, k_B is the Boltzmann constant, and $\mathrm{DOS}(E)$ is the density of states of graphene [32]. The reduction of ξ with n_D implies the size of the sp^2 domain decreases as the extent of oxidation increases [14,41]. On the other hand, charge transport in GO samples with smaller $n_D = 0.23$ and 0.39×10^{12} cm^{-2} is not explained by 2D VRH or a thermal activation model. To investigate the charge transport at metal–insulator boundaries in more detail, we prepared an additional GO FET with $n_D = 0.8 \times 10^{12}$ cm^{-2} in a Hall-bar geometry shown in Figure 1b and studied the four-probe conductivity between $2 < T < 300$ K. Figure 5b plots $\log \sigma$ of GO with $n_D = 0.8 \times 10^{12}$ cm^{-2} as a function of $T^{-1/3}$. Whereas for $15 < T < 145$ K, $\log \sigma$ is linearly proportional to $T^{-1/3}$ and agrees well with the 2D VRH model, σ is a little larger than the linear fitting curve for $145 < T < 300$ K as shown in the inset of Figure 5b. Additionally, σ becomes saturated for $2 < T < 15$ K, deviating from the linear dependence.
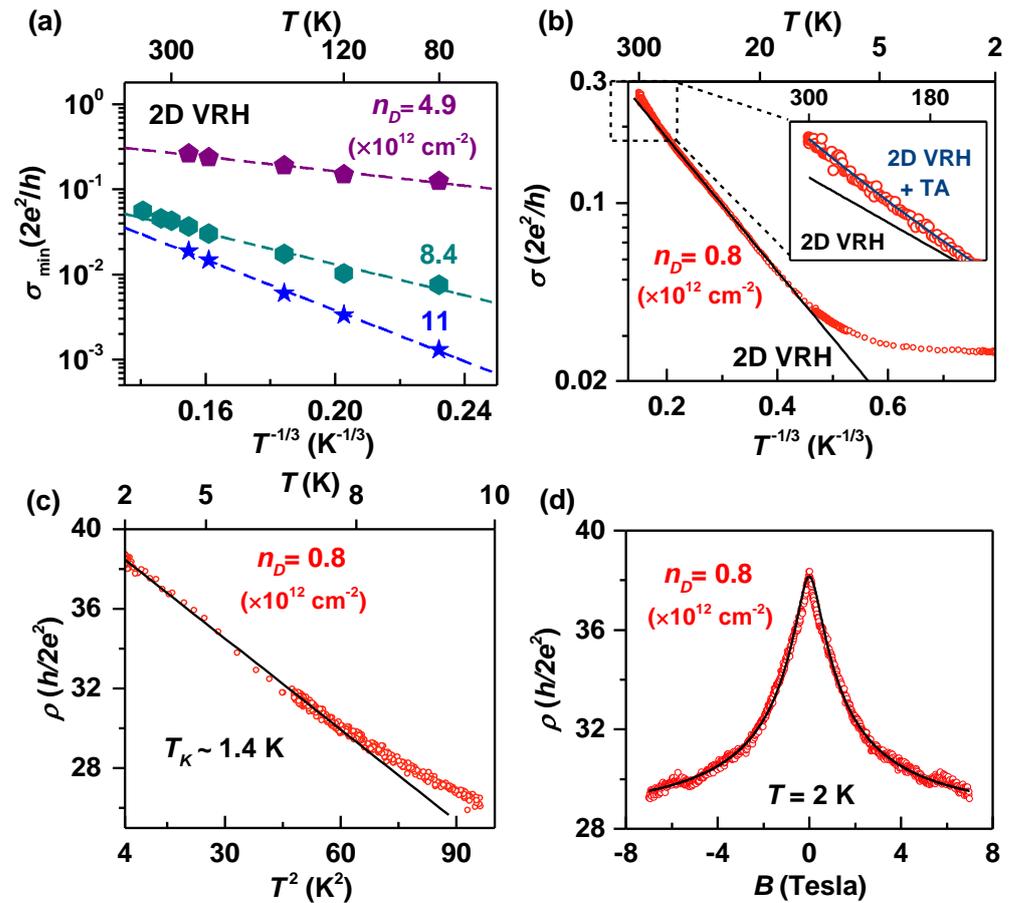
Figure 5. (**a**) $\log \sigma_{min}$ vs. $T^{-1/3}$ for graphene oxides with $n_D = 4.9$, 8.4, and 11×10^{12} cm^{-2}. (**b**) $\log \sigma$ vs. $T^{-1/3}$ for graphene oxide with $n_D = 0.8 \times 10^{12}$ cm^{-2}, measured between $2 < T < 300$ K. For $15 < T < 145$ K, $\log \sigma$ is linearly proportional to $T^{-1/3}$ and agrees well with 2D VRH model. (Inset) $\log \sigma$ vs. $T^{-1/3}$, zoomed in for $300 < T < 140$ K. The data are best fitted considering both 2D VRH and thermal activation conduction. (**c**) ρ vs. T^2 in the low T regime for $2 < T < 10$ K for GO with $n_D = 0.8 \times 10^{12}$ cm^{-2}. (**d**) Magnetoresistance of the graphene oxide with $n_D = 0.8 \times 10^{12}$ cm^{-2}, measured at $T = 2$ K.

In the temperature range of $145 < T < 300$ K, the T-dependence of the conductivity can be explained by considering 2D VRH and thermal activation conduction (TA) together. The data are fitted well with $\sigma = \sigma_0 \exp\left(\frac{T_0}{T}\right)^{\frac{1}{3}} + \sigma_1 \exp\left(\frac{E_a}{k_B T}\right)$, as seen from the inset of Figure 5b, and an activation energy of $E_a \simeq 47$ meV is obtained. This value is larger than $E_g \simeq 27$ meV inferred from Figure 3d and can be associated with the influence of the $e - h$ puddle ($\delta E_{e-h} \simeq 78$ meV). The saturation of σ below $T < 15$ K is analyzed by considering the Kondo effect and presented in Figure 5c. The Kondo effect occurs when the charge carriers interact with the local magnetic moment of defects and the T-dependence of electrical resistivity ρ is given as follows in the low-temperature regime [42].

$$\rho = \rho_c + \rho_K \left[1 - \left(\frac{\pi}{2}\right)^4 \left(\frac{T}{T_K}\right)^2 \right] \quad (3)$$

Here, ρ_K is the Kondo resistivity at 0 K, and ρ_c is the temperature-independent resistivity parameter. T_K is the Kondo temperature, and the stronger the coupling between the magnetic moment and the charge carrier, the greater the value of T_K [42]. In Figure 5c, ρ is plotted versus T^2, and $\rho_K \simeq 20 \frac{h}{e^2}$, $\rho_c \simeq 0.049 \frac{h}{e^2}$ and $T_K = 1.4$ K are deduced from a linear

fit. The obtained value of T_K = 1.4 K suggests rather weak coupling between the magnetic moment of defects and charge carriers in UV-oxidized graphene with $n_D = 0.8 \times 10^{12}$ cm^{-2}.

Figure 5d shows the magnetoresistance (MR) of the graphene oxide at $n_D = 0.8 \times 10^{12}$ cm^{-2}, measured at $T = 2$ K. A negative MR was observed in which ρ decreased as the magnetic field B increased up to 7 teslas. The negative MR is analyzed with the following equation [43] including both strong and weak localization effects.

$$\frac{\rho(B) - \rho(0)}{\rho(0)} = \frac{l_\phi}{l_c} \left[\frac{\Psi\left(\frac{2B_c + B_\phi + B_e}{B} + \frac{1}{2}\right) - \Psi\left(\frac{B_c + B_\phi}{B} + \frac{1}{2}\right)}{\ln\left(1 + \frac{B_e}{B_c + B_\phi}\right)} - 1 \right] \qquad (4)$$

Here, $\Psi(x)$ is the digamma function, and the characteristic length l_i is related to the characteristic magnetic field $\left(B_{(i=c,\phi,e)} = \frac{\hbar}{4el_i^2}\right)$. A localization length of $l_c \simeq 160$ nm, phase coherence length of $l_\phi \simeq 46$ nm, and elastic scattering length of $l_e \simeq 13$ nm are obtained from the fitting of Equation (4) to the MR data. l_ϕ is three times smaller than l_c, implying a dominant role of weak localization in the negative MR for the GO with $n_D = 0.8 \times 10^{12}$ cm^{-2}.

4. Conclusions

In summary, we have prepared graphene-oxide FETs with different degrees of oxidation by controlling the UV irradiation time on graphene, and investigated the charge transport and the evolution of the transport gap according to the extent of oxidation. With increasing oxygenous defect density n_D, the charge transport transitioned from ballistic to diffusive conduction around $n_D \simeq 10^{12}$ cm^{-2} and the transport gap grew in proportion to $\sqrt{n_D}$. Taking into account the potential fluctuation related to the the $e - h$ puddle, we suggested the bandgap of GO to be $E_g \simeq 30\sqrt{n_D\,(10^{12}\ \text{cm}^{-2})}$ meV. The temperature dependence of the conductivity showed metal–insulator transitions at $n_D \simeq 0.3 \times 10^{12}$ cm^{-2} at the point where $k_F l \simeq 1$, which meets the Ioffe–Regel criterion. For GO with $n_D \geq 4.9 \times 10^{12}$ cm^{-2}, analysis indicated charge transport occurred via 2D variable range hopping conduction between localized sp^2 domains with the localization length decreasing with n_D. Finally, the Kondo effect and negative MR in the low-temperature regime were studied in GO with $n_D = 0.8 \times 10^{12}$ cm^{-2}.

Author Contributions: Conceptualization, H.Y.L. and S.H.J.; formal analysis, H.Y.L. and S.H.J.; investigation, H.Y.L.; resources, H.Y.L., M.M.H., E.H.K., J.S.C., and B.H.P.; writing—original draft preparation, H.Y.L. and S.H.J.; writing—review and editing, H.Y.L., S.H.J., and E.E.B.C.; visualization, H.Y.L. and S.H.J.; supervision, H.Y.L. and S.H.J.; project administration, H.Y.L. and S.H.J.; funding acquisition, S.H.J. All authors have read and agreed to the published version of the manuscript.

Institutional Review Board Statement: Not applicable.

Informed Consent Statement: Not applicable.

Data Availability Statement: Not applicable.

Conflicts of Interest: The authors declare no conflict of interest.

References

1. Novoselov, K.S.; Geim, A.K.; Morozov, S.V.; Jiang, D.E.; Zhang, Y.; Dubonos, S.V.; Grigorieva, I.V.; Firsov, A.A. Electric field effect in atomically thin carbon films. *Science* **2004**, *306*, 666–669. [CrossRef] [PubMed]
2. Morozov, S.; Novoselov, K.; Katsnelson, M.; Schedin, F.; Elias, D.C.; Jaszczak, J.A.; Geim, A. Giant intrinsic carrier mobilities in graphene and its bilayer. *Phys. Rev. Lett.* **2008**, *100*, 016602. [CrossRef] [PubMed]
3. Shen, H.; Shi, Y.; Wang, X. Synthesis, charge transport and device applications of graphene nanoribbons. *Synth. Met.* **2015**, *210*, 109–122. [CrossRef]
4. Craciun, M.; Khrapach, I.; Barnes, M.; Russo, S. Properties and applications of chemically functionalized graphene. *J. Phys. Condens. Matter* **2013**, *25*, 423201. [CrossRef]

5.   Ahmad, Y.; Batisse, N.; Chen, X.; Dubois, M. Preparation and Applications of Fluorinated Graphenes. *C* **2021**, *7*, 20. [CrossRef]
6.   Whitener, K.E., Jr. Hydrogenated graphene: A user's guide. *J. Vac. Sci. Technol. A Vacuum Surf. Film.* **2018**, *36*, 05G401. [CrossRef]
7.   Jin, Y.; Zheng, Y.; Podkolzin, S.G.; Lee, W. Band gap of reduced graphene oxide tuned by controlling functional groups. *J. Mater. Chem. C* **2020**, *8*, 4885–4894. [CrossRef]
8.   Yan, J.A.; Xian, L.; Chou, M. Structural and electronic properties of oxidized graphene. *Phys. Rev. Lett.* **2009**, *103*, 086802. [CrossRef]
9.   Nourbakhsh, A.; Cantoro, M.; Vosch, T.; Pourtois, G.; Clemente, F.; van der Veen, M.H.; Hofkens, J.; Heyns, M.M.; De Gendt, S.; Sels, B.F. Bandgap opening in oxygen plasma-treated graphene. *Nanotechnology* **2010**, *21*, 435203. [CrossRef]
10.   Lundie, M.; Šljivančanin, Ž.; Tomić, S. Analysis of energy gap opening in graphene oxide. *J. Phys. Conf. Ser.* **2014**, *526*, 012003.
11.   Zhu, Y.; Murali, S.; Cai, W.; Li, X.; Suk, J.W.; Potts, J.R.; Ruoff, R.S. Graphene and graphene oxide: Synthesis, properties, and applications. *Adv. Mater.* **2010**, *22*, 3906–3924. [CrossRef]
12.   Pei, S.; Cheng, H.M. The reduction of graphene oxide. *Carbon* **2012**, *50*, 3210–3228. [CrossRef]
13.   Eda, G.; Mattevi, C.; Yamaguchi, H.; Kim, H.; Chhowalla, M. Insulator to semimetal transition in graphene oxide. *J. Phys. Chem. C* **2009**, *113*, 15768–15771. [CrossRef]
14.   Negishi, R.; Akabori, M.; Ito, T.; Watanabe, Y.; Kobayashi, Y. Band-like transport in highly crystalline graphene films from defective graphene oxides. *Sci. Rep.* **2016**, *6*, 28936. [CrossRef]
15.   Liu, L.; Xie, D.; Wu, M.; Yang, X.; Xu, Z.; Wang, W.; Bai, X.; Wang, E. Controlled oxidative functionalization of monolayer graphene by water-vapor plasma etching. *Carbon* **2012**, *50*, 3039–3044. [CrossRef]
16.   Mulyana, Y.; Uenuma, M.; Ishikawa, Y.; Uraoka, Y. Reversible oxidation of graphene through ultraviolet/ozone treatment and its nonthermal reduction through ultraviolet irradiation. *J. Phys. Chem. C* **2014**, *118*, 27372–27381. [CrossRef]
17.   Haidari, M.M.; Kim, H.; Kim, J.H.; Park, M.; Lee, H.; Choi, J.S. Doping effect in graphene-graphene oxide interlayer. *Sci. Rep.* **2020**, *10*, 8258. [CrossRef]
18.   Osofsky, M.; Hernández, S.; Nath, A.; Wheeler, V.; Walton, S.; Krowne, C.; Gaskill, D. Functionalized graphene as a model system for the two-dimensional metal-insulator transition. *Sci. Rep.* **2016**, *6*, 19939. [CrossRef]
19.   Ryu, G.H.; Lee, J.; Kang, D.; Jo, H.J.; Shin, H.S.; Lee, Z. Effects of dry oxidation treatments on monolayer graphene. *2D Mater.* **2017**, *4*, 024011. [CrossRef]
20.   Yang, X.; Yan, M. Removing contaminants from transferred CVD graphene. *Nano Res.* **2020**, *13*, 599–610. [CrossRef]
21.   Eckmann, A.; Felten, A.; Verzhbitskiy, I.; Davey, R.; Casiraghi, C. Raman study on defective graphene: Effect of the excitation energy, type, and amount of defects. *Phys. Rev. B* **2013**, *88*, 035426. [CrossRef]
22.   Ferrari, A.C.; Basko, D.M. Raman spectroscopy as a versatile tool for studying the properties of graphene. *Nat. Nanotechnol.* **2013**, *8*, 235–246. [CrossRef]
23.   Anno, Y.; Takeuchi, M.; Matsuoka, M.; Takei, K.; Akita, S.; Arie, T. Effect of defect-induced carrier scattering on the thermoelectric power of graphene. *Appl. Phys. Lett.* **2017**, *110*, 263501. [CrossRef]
24.   Childres, I.; Jauregui, L.A.; Tian, J.; Chen, Y.P. Effect of oxygen plasma etching on graphene studied using Raman spectroscopy and electronic transport measurements. *New J. Phys.* **2011**, *13*, 025008. [CrossRef]
25.   Pollard, A.J.; Brennan, B.; Stec, H.; Tyler, B.J.; Seah, M.P.; Gilmore, I.S.; Roy, D. Quantitative characterization of defect size in graphene using Raman spectroscopy. *Appl. Phys. Lett.* **2014**, *105*, 253107. [CrossRef]
26.   Wang, Z.; Yao, Q.; Eigler, S. Room-temperature transport properties of graphene with defects derived from oxo-graphene. *Chem.-Eur. J.* **2020**, *26*, 6484–6489. [CrossRef] [PubMed]
27.   Zhong, J.H.; Zhang, J.; Jin, X.; Liu, J.Y.; Li, Q.; Li, M.H.; Cai, W.; Wu, D.Y.; Zhan, D.; Ren, B. Quantitative correlation between defect density and heterogeneous electron transfer rate of single layer graphene. *J. Am. Chem. Soc.* **2014**, *136*, 16609–16617. [CrossRef]
28.   Bolotin, K.I.; Sikes, K.J.; Hone, J.; Stormer, H.; Kim, P. Temperature-dependent transport in suspended graphene. *Phys. Rev. Lett.* **2008**, *101*, 096802. [CrossRef] [PubMed]
29.   Di Bartolomeo, A. Graphene Schottky diodes: An experimental review of the rectifying graphene/semiconductor heterojunction. *Phys. Rep.* **2016**, *606*, 1–58. [CrossRef]
30.   Chen, J.H.; Cullen, W.G.; Jang, C.; Fuhrer, M.; Williams, E.D. Defect scattering in graphene. *Phys. Rev. Lett.* **2009**, *102*, 236805. [CrossRef]
31.   Chen, J.H.; Jang, C.; Adam, S.; Fuhrer, M.; Williams, E.D.; Ishigami, M. Charged-impurity scattering in graphene. *Nat. Phys.* **2008**, *4*, 377–381. [CrossRef]
32.   Moser, J.; Tao, H.; Roche, S.; Alzina, F.; Torres, C.S.; Bachtold, A. Magnetotransport in disordered graphene exposed to ozone: From weak to strong localization. *Phys. Rev. B* **2010**, *81*, 205445. [CrossRef]
33.   Eigler, S.; Enzelberger-Heim, M.; Grimm, S.; Hofmann, P.; Kroener, W.; Geworski, A.; Dotzer, C.; Röckert, M.; Xiao, J.; Papp, C.; et al. Wet chemical synthesis of graphene. *Adv. Mater.* **2013**, *25*, 3583–3587. [CrossRef]
34.   Abanin, D.A.; Shytov, A.; Levitov, L. Peierls-type instability and tunable band gap in functionalized graphene. *Phys. Rev. Lett.* **2010**, *105*, 086802. [CrossRef]
35.   Sehrawat, P.; Islam, S.; Mishra, P.; Ahmad, S. Reduced graphene oxide (rGO) based wideband optical sensor and the role of Temperature, Defect States and Quantum Efficiency. *Sci. Rep.* **2018**, *8*, 3537.
36.   Adam, S.; Hwang, E.; Galitski, V.; Sarma, S.D. A self-consistent theory for graphene transport. *Proc. Natl. Acad. Sci. USA* **2007**, *104*, 18392–18397. [CrossRef]

37. Gallagher, P.; Todd, K.; Goldhaber-Gordon, D. Disorder-induced gap behavior in graphene nanoribbons. *Phys. Rev. B* **2010**, *81*, 115409. [CrossRef]

38. Stampfer, C.; Güttinger, J.; Hellmüller, S.; Molitor, F.; Ensslin, K.; Ihn, T. Energy gaps in etched graphene nanoribbons. *Phys. Rev. Lett.* **2009**, *102*, 056403. [CrossRef]

39. Adam, S.; Cho, S.; Fuhrer, M.; Sarma, S.D. Density inhomogeneity driven percolation metal-insulator transition and dimensional crossover in graphene nanoribbons. *Phys. Rev. Lett.* **2008**, *101*, 046404. [CrossRef]

40. Sarma, S.D.; Hwang, E. Two-dimensional metal-insulator transition as a strong localization induced crossover phenomenon. *Phys. Rev. B* **2014**, *89*, 235423. [CrossRef]

41. Vianelli, A.; Candini, A.; Treossi, E.; Palermo, V.; Affronte, M. Observation of different charge transport regimes and large magnetoresistance in graphene oxide layers. *Carbon* **2015**, *89*, 188–196. [CrossRef]

42. Chen, J.H.; Li, L.; Cullen, W.G.; Williams, E.D.; Fuhrer, M.S. Tunable Kondo effect in graphene with defects. *Nat. Phys.* **2011**, *7*, 535–538. [CrossRef]

43. Hilke, M.; Massicotte, M.; Whiteway, E.; Yu, V. Weak localization in graphene: Theory, simulations, and experiments. *Sci. World J.* **2014**, *2014*, 737296. [CrossRef] [PubMed]